PAPER • OPEN ACCESS

Identifying coherent structures and vortex clusters in Taylor-Couette turbulence

To cite this article: Vamsi Spandan *et al* 2016 *J. Phys.: Conf. Ser.* **708** 012006

View the article online for updates and enhancements.

Identifying coherent structures and vortex clusters in Taylor-Couette turbulence

Vamsi Spandan, Rodolfo Ostilla-Monico, Detlef Lohse, Roberto Verzicco

Physics of Fluids, Mesa+ Institute, Faculty of Science and Technology, University of Twente, Postbus 217, 7500AE Enschede

E-mail: `vamsispandan@gmail.com`

Abstract. The nature of the underlying structures in Taylor-Couette (TC) flow, the flow between two co-axial and independently rotating cylinders is investigated by two methods. First, the quadrant analysis technique for identifying structures with intense radial-azimuthal stresses (also referred to as 'Q's) of Lozano-Durán *et al.*, (*J. Fluid Mech.* 694, 100-130) is used to identify the main structures responsible for the transport of angular velocity. Second, the vortex clusters are identified based on the analysis by del Álamo *et al.*, (*J. Fluid. Mech.*, 561, 329-358). In order to test these criteria, two different radius ratios $\eta = r_i/r_o$ are considered, where r_i and r_o are the radii of inner and outer cylinder, respectively: (i) $\eta = 0.5$ and (ii) $\eta = 0.909$, which correspond to high and low curvature geometries, respectively and have different underlying structures. The Taylor rolls, i.e. the large-scale coherent structures, are effectively captured as 'Q's for the low curvature setup and it is observed that curvature plays a dominant role in influencing the size and volumes of these 'Q's. On the other hand, the vortex clusters are smaller in size when compared to the 'Q' structures. These vortex clusters are found to be taller in the case of $\eta = 0.909$, while the distribution of the lengths of these clusters is almost homogenous for both radius ratios.

1. Introduction

The ubiquitous nature of wall bounded turbulent flows both in nature and in process technology makes them a subject of interest for fundamental scientific research as well as for industrial applications. Since its earliest observation, turbulence has been always described as a process of random and chaotic mixing [1]. Turbulent wall flows [2] are dominated by complex multi-scale processes in which momentum (and other quantities such as mass or heat) are transported between the wall and the bulk of the flow and vice versa. However, even in the apparent disorder of turbulence, researchers have found the existence of some 'order' or, in other words, coherence in turbulent flows. In particular, for wall-bounded turbulent flows, the existence of various types of coherent structures such as hairpins, horse-shoe vortices, herringbone-like streaks, and many others has been the subject of research in several pioneering studies [3, 4, 5]. With consistent increase in computational capabilities, many advances have been made in understanding the role the underlying structures play in the turbulent cascades where energy and momentum are transferred across length and time scales [6].

Most studies of wall-bounded turbulence have been limited to the canonical case of pressure-driven flow between either two parallel plates or inside a pipe (hereafter referred to as a channel-

and pipe-flow, respectively) due to their simplicity and ease to conduct numerical simulations and high precision experiments. While much insight has been gained from these systems, it is not yet clear if the coherent structures and cascade processes present in these flows are universal. Simulations and experiments of other canonical flows, such as the zero-pressure-gradient boundary layer and the flow between two parallel-plates driven by shear (hereafter referred to as plane Couette (PC)) have taken off in the last years, and are raising interesting questions on the universality of wall-bounded turbulence. In particular, recent numerical simulations of the Taylor-Couette (TC) problem, i.e. the flow between two independently rotating co-axial cylinders have shown that some of the features occuring in channel flow are not present in TC flow. For example, in TC flow in many areas of the parameter space large-scale structures appear. These are known as Taylor rolls, and are fixed in space, persistent in time, and are responsible for majority of the angular momentum transport [7]. This is in contrast to channel flows, where analysis based on cospectra show that the large-scale wall-attached structures are inactive [6]. Even for PC flows, this cospectra analysis has shown that large-scale wall-attached structures are inactive [8].

TC flow can be described using four non-dimensional parameters: two for the geometry, i.e. the radius ratio $\eta = r_i/r_o$, where r_i and r_o are the radii of the inner and outer cylinders, respectively and the aspect ratio $\Gamma = L_z/d$, where L_z is the axial length of the cylinders while $d = r_o - r_i$ is the gap-width, and two other parameters which relate to the strength of the driving, and are usually taken in terms of the inner- and outer cylinder Reynolds numbers as $Re_i = U_i d/\nu$ and $Re_o = U_o d/\nu$ where U_i and U_o are inner and outer cylinder velocities, respectively, and ν the kinematic viscosity of the fluid. We use a cylindrical coordinate system (r, θ, z) to mathematically tract TC flow, with u_r, u_θ and u_z are the three velocities: radial (corresponding to wall-normal in channel flow), azimuthal (streamwise) and axial (spanwise). The angular velocity ω is simply $\omega = u_\theta/r$. From a geometrical point of view, the curvature of the wall present in TC flow is one of the major factors responsible for the differences between the dynamics of TC flow and other canonical flows. Studies of boundary layers over curved surfaces [9, 10, 11] have shown that even a small curvature added to the channel flow can be responsible for major changes in the flow dynamics. From the point of view of the driving there is another difference: channel flow is pressure driven while TC flow (and PC flow) are shear driven. Also, unlike the two other flows, TC flow is linearly unstable if $d|\mathcal{L}|/dr^2 < 0$, where r is the radial coordinate and $\mathcal{L}$ is the angular momentum. When the driving exceeds a critical value, the instability gives rise to the formation of laminar Taylor rolls which fill the gap between both cylinders. With further increase in driving the laminar Taylor rolls transition into wavy Taylor rolls, and eventually into fully turbulent Taylor rolls. As mentioned previously, these rolls are persistent in both space and time in some regions of the (η, Re_i, Re_o) parameter space, and have been observed in both experiments and numerical simulations. Even at $Re_i \sim 10^6$, they can remain coherent at large-scales, and are responsible for majority of the angular momentum transport [7, 12, 13].

The geometry of the setup, and especially the radius ratio dictates the strength and coherence of the Taylor rolls. For pure inner cylinder rotation, it has been observed that when the curvature is low (i.e. η=0.909), strong signatures of the Taylor rolls exist not only in spectra and correlations, but also in the azimuthally- and time-averaged fields. The strength of the rolls are diminished in systems with higher curvature (i.e. η=0.5), an effect which can be attributed to the strong asymmetry between the inner and outer cylinders when $\eta = 0.5$ [14, 13, 7]. Adding a slight counter-rotation can make the large-scale structures reappear, as was seen in the TC experiments by van der Veen *et al.* [15], who for $\eta = 0.5$ found some signatures of large-scale coherent structures when the cylinders were counter-rotating but none for pure inner-cylinder rotation. The aspect ratio Γ controls the wavelength of the rolls, as only a even amount of rolls of the domain can fit. However, different roll wavelengths do not give very different flow physics

Table 1. Details of the numerical simulations. The first column is the radius ratio η. The second to fourth columns represent the amount of grid points in the azimuthal, radial and axial directions, the sixth and seventh columns show the length of the domain in the azimuthal (streamwise) and axial (spanwise) directions at the mid-gap, where $L_x = \pi(r_i + r_o)/n_s$. The seventh column shows the frictional Reynolds number at the inner cylinder, while the ninth and tenth columns show the resolution in inner wall-units at the mid-gap.

η	N_θ	N_r	N_z	$L_x/(2d)$	$L_z/(2d)$	$Re_{\tau,i}$	Δx^+	Δz^+
0.5	768	768	512	6.2	4.2	200	1.6	1.6
0.909	1024	768	512	6.5	4.2	380	2.6	3.1

if the driving is large enough [13].

The main focus of this study is to find more advanced ways of quantifying the large-scale coherent structures in TC, and to verify that they can be captured not only in time averaged flow fields and velocity spectra, but also through other methods by considering a single snapshot of the flow field, or a time series of snapshots sufficiently separated in time. A number of studies exist in the literature which elucidate the various techniques that can be used to identify organized 'structures' or 'clusters' in a turbulent flow field; in particular here we focus on the 'quadrant' analysis technique [16, 17, 18] and the identification of vortex clusters [19]. del Álamo et al. [20] adopted the approach of Chong et al. [19] based on the velocity gradient discriminant to identify clusters of vortical structures in a turbulent channel flow. For a similar flow configuration, Lozano-Durán et al. [21] studied the properties of three dimensional intense Reynolds stress structures (hereafter referred to as 'Q' structures) in line with the one-dimensional quadrant analysis of Lu and Willmarth [17]. In this work we follow the approach of Lozano-Durán et al. [21] and of del Álamo et al. [20] to identify both 'Q' structures and vortex clusters in a turbulent TC flow. In particular, the analysis of Lozano-Durán et al. is interesting for TC because it comes to different conclusions about the large-scale wall-attached structures in channels, namely that they actively transport Reynolds stresses, similar to the Taylor-rolls.

In order to obtain the flow field snapshots, direct numerical simulations of TC flow were performed using a second-order central finite-difference scheme with fractional time stepping [22, 23]. This scheme has already been tested and used extensively to study the dynamics of TC flow over a wide parameter range [24, 25, 26, 14]. As mentioned previously, for the purpose of this study two different radius ratios of the TC setup were considered, namely (i) $\eta = 0.5$ (high curvature) and (ii) $\eta = 0.909$ (low curvature). The aspect ratio for both setups is fixed to $\Gamma = 2.09$ so the domain can accommodate a single Taylor roll pair. To reduce computational costs, for $\eta = 0.5$, a rotational symmetry of $n_s = 3$ was used, while for $\eta = 0.909$ we took $n_s = 20$. These two rotational symmetries ensure that the azimuthal length of the domain is of the order of 2π half-gaps. Full details of the numerical resolution used is presented in Table 1. The outer cylinder is kept at rest (i.e. $Re_o = 0$) and the inner cylinder is rotated to reach a Reynolds number of $Re_i = 2 \times 10^4$, which corresponds to a frictional Reynolds number at the inner cylinder of approximately $Re_{\tau,i} = 200$ and $Re_{\tau,i} = 380$ for $\eta = 0.5$ and $\eta = 0.909$, respectively. For $\eta = 0.5$, the dynamics of the TC flow is dominated by the asymmetry between both the cylinders while for $\eta = 0.909$, although the curvature is much smaller it is sufficient enough for the linear instability to give rise to Taylor rolls. Three snapshots of the flow field separated by at least ten large-eddy turnover times d/U_i are selected for each radius ratio, to ensure that the statistics are not dependent on the selected snapshot.
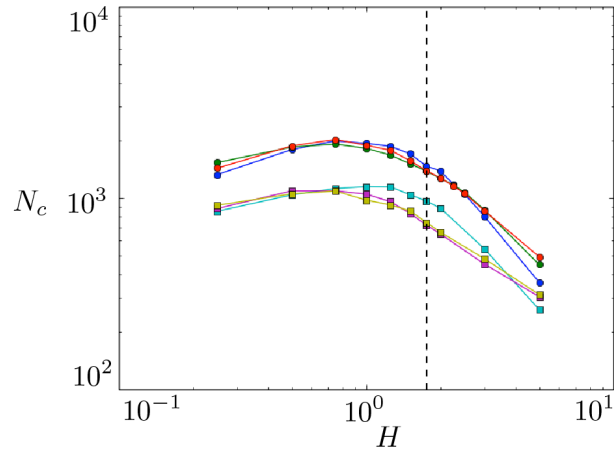
Figure 1. Total number of identified 'Q' structures for $\eta = 0.909$ (squares) and $\eta = 0.5$ (circles); three different snapshots are considered. The vertical line marks the chosen threshold ($H = 1.75$)

The manuscript is organized as follows: section 2 deals with the procedure for identifying 'Q's, which are responsible for transport of tangential Reynolds stresses. These structures are identified with the Taylor-roll for the low curvature case. Some aspect of these 'Q's are also quantified. Section 3 is about the identification and statistics of vortex clusters, with a focus on the geometry and dissipation. Section 4 is a summary of the present work and an outlook for the future.

2. 'Q' structures

2.1. Identification and percolation analysis

In this section we focus on the 'Q's, i.e. the structures responsible for the transport of Reynolds stresses. In TC flow the transported (and conserved) quantity is the angular velocity flux J^ω which is defined as $J^\omega = r^3(\langle u_r\omega\rangle_{A,t} - \nu\partial_r\langle\omega\rangle_{A,t})$, where $\langle...\rangle_{A,t}$ represents averaging in the two homogenous (azimuthal and axial) directions and in time and u_r and ω are the radial velocity and angular velocity, respectively [27]. In the definition of J^ω, the first term represents the Reynolds stress contribution while the second term is the viscous contribution to the angular velocity transport. We note that this equation is analogous to the definition of the total stress in channels, with the difference that the torque (stress) is constant throughout the domain, as the flow is shear driven.

Following the approach of Lozano-Durán *et al.* [21] the 'Q' structures in the case of TC flow are defined as connected regions satisfying the following criterion:

$$|u_r u_\theta| > H u_r' u_\theta'. \tag{1}$$

where H is the hyperbolic hole size and can be thought of as a threshold parameter for the 'Q' structures, u_r, u_θ are the instantaneous radial and azimuthal velocities while u_r', u_θ' are the root mean square fluctuations respectively. Connectivity of the vortex clusters is defined in terms of its six neighbouring grid points and any object smaller than 30^3 wall units in volume is filtered out for the analysis.

The first step in identifying the relevant 'Q' structures and vortex clusters is to perform a percolation analysis to calculate the best threshold parameters, i.e. H. Thresholding parameters have to be chosen carefully, especially in an inhomogenous flow such as wall bounded turbulence.
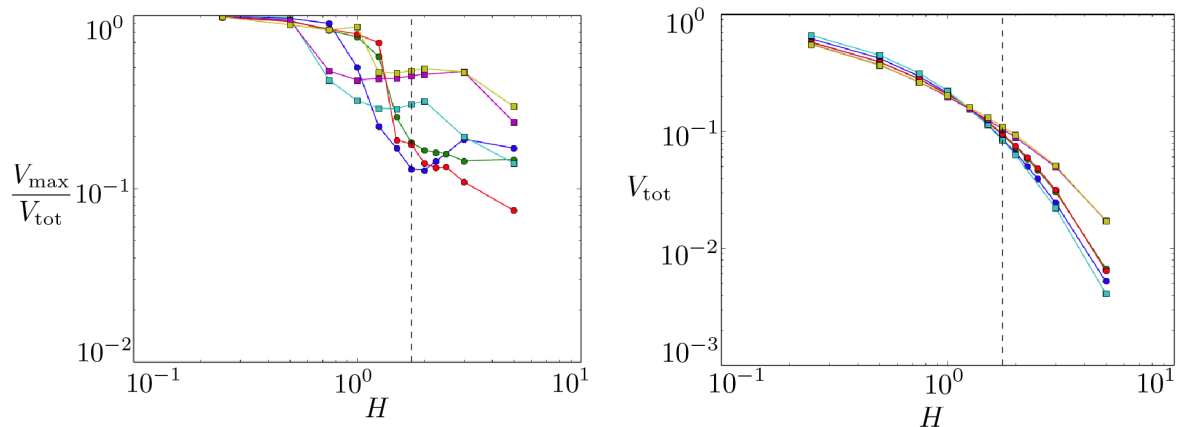
Figure 2. Left panel: Maximum volume of a 'Q' normalised by the total volume of all the identified 'Q' s in the domain. Right panel: Total volume of all the identified 'Q' s normalised by the volume of the TC domain. Square symbols refer to $\eta = 0.909$, while the circles refer to $\eta = 0.5$. Three different snapshots for each radius ratio are considered.

In figure 1 we plot the total number N_c of identified 'Q' structures for both radius ratios and the three different snapshots. At a high value of ($H \sim 3$) the number of structures identified are of the order $N_c \sim \mathcal{O}(10^2)$. On decreasing the value of H, more structures arise while the structures grow in size (this can also be seen in the left panel of figure 2). Further decreasing H just results in the structures merging together without increasing in size until a single structure fills up the entire volume. Another interesting aspect is that the total number of identified 'Q's in the TC flow ($N_c \sim \mathcal{O}(10^3)$) is much smaller than what was previously seen for channel flow (i.e. $N_c \sim \mathcal{O}(10^6)$) by Lozano-Durán *et al.* [21]. Since this cannot be accounted for only due to computational box-size difference, it indicates either the existence of larger 'Q' s in TC flow, or that the 'Q' s fill a smaller part of the domain.

In the left panel of figure 2 we plot the volume of the largest 'Q' structure normalized by the total volume of all identified 'Q's for different values of H. We observe that the percolation behaviour of the 'Q's in TC flow is very similar to that seen in channel flow by Lozano-Durán *et al.* [21]. When $H > 2$, there is no significant change in the volume of the largest structures computed, while a percolation crisis (recognized by the steepest gradient in the plot of the normalized maximum volume of the structures) occurs for $0.7 < H < 2$ (c.f. left panel of figure 2). The steep fall in the maximum volume is not very obvious for $\eta = 0.909$ and it occurs at a smaller value of H when compared to the cases with $\eta = 0.5$. As noted before, on further decreasing H all the 'Q's merge into a single structure. A percolation threshold of $H = 1.75$ is thus chosen for identifying the 'Q' structures (shown as a vertical dotted line in figures 2 and 1). The right panel of figure 2 shows the total volume of all the identified 'Q' structures normalized by the total volume of the TC domain. We can observe that while there is some difference at high values of H, the curves overlap for most of the range of H where the percolation crisis occurs. In this way, we ensure that the selected snapshot does not have an influence on subsequent analysis. However, we note that quite some variation exists across snapshots, and by using only three snapshots we might be incurring in some statistical errors.

2.2. Visualization of structures
In figure 3 we show a visualisation of the 'Q' structures for two different radius ratios and also the averaged contour plots of the azimuthal velocity. When the curvature of the setup
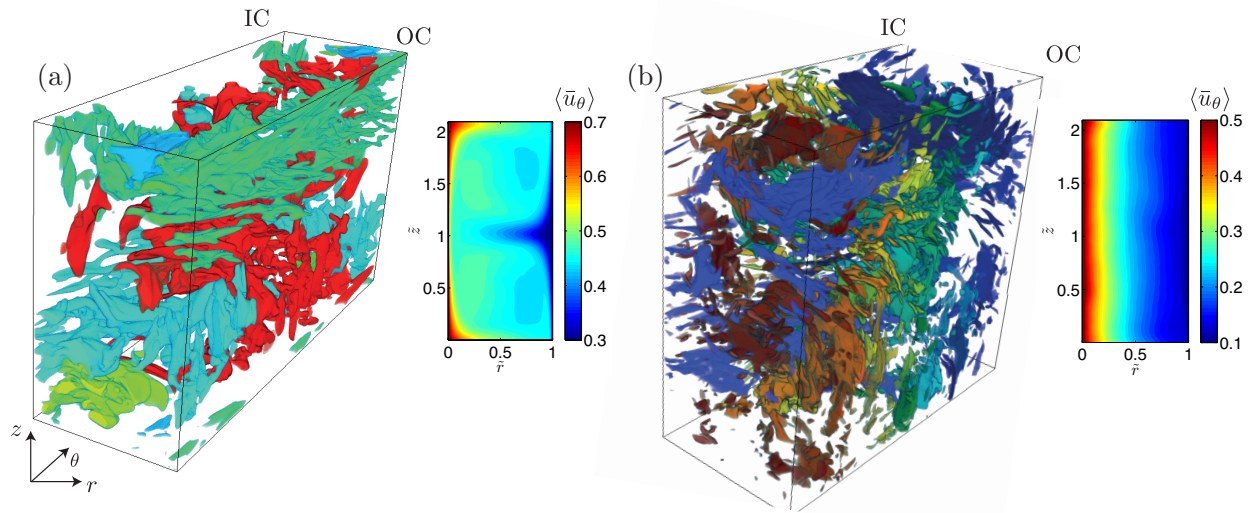
Figure 3. 'Q' structures identified for two different radius ratios (a) $\eta = 0.909$ (b) $\eta = 0.5$. The right panels show azimuthally and time averaged contour plots of azimuthal velocity. For both cases $H = 1.75$

is low (figure 3a), the averaged contours of azimuthal velocity show a strong signature of the coherent Taylor rolls (one-pair here). The Taylor rolls can also be visually seen through a three dimensional volume plot of the 'Q' structures calculated using the criterion introduced in equation 1. Indeed, in figure 3a we can observe large scale structures (identified by different colours) which occupy most of the volume. These large scale structures, co-exist with other small scale structures such as near wall streaks. However, most of these small structures, including 'Q 's from every quadrant, eventually merge into a large-scale Taylor roll. For very low values of H, the large 'Q 's merge with the smaller ones to fill the TC domain completely as seen in the right panel of figure 2.

Figure 3b shows the case of a high curvature setup, where the rolls seem to break up, and there is no clear signature of a large scale roll both in the averaged contour plot and also from the visualisation of the 'Q' structures. Nonetheless, some large scale structures still exist which may correspond to the plume ejections from the inner cylinder. We study the nature of these structures while analysing the distribution of 'Q' s later. It seems that while some small scale structures are preserved in both systems, the roll structure observed in the case of $\eta = 0.909$ breaks up into multiple 'Q's when the curvature is high i.e. $\eta = 0.5$. This is also reflected in figure 1 where the total number of 'Q's identified is higher for $\eta = 0.5$ when compared to the case with $\eta = 0.909$, again a difference higher than what can be accounted for by the difference in computational box size. Using the quadrant analysis technique allows us to classify the identified structures into various categories such as Q_1 (outward interactions), Q_2 (ejections), Q_3 (inward interactions) and Q_4 (sweeps) based on the volume integral of the stream-wise and wall-normal fluctuations over a single structure. The mean stream-wise and wall-normal fluctuation in a structure is computed as $u_m = \frac{\int u dV}{\int dV}$ and $v_m = \frac{\int v dV}{\int dV}$; the structure is termed Q_1 if $u_m > 0$ and $v_m > 0$, Q_2 if $u_m < 0$ and $v_m > 0$, Q_3 if $u_m < 0$ and $v_m < 0$, and Q_4 when $u_m > 0$ and $v_m < 0$. In order to study how the distribution of these structures depends on the curvature of the setup we categorise the various 'Q's in table 2 for $\eta = 0.5$ and $\eta = 0.909$. For channel

Table 2. Distribution of the 'Q' structures computed over three different snapshots for the low-curvature ($\eta = 0.5$) and high-curvature ($\eta = 0.909$) setup respectively.

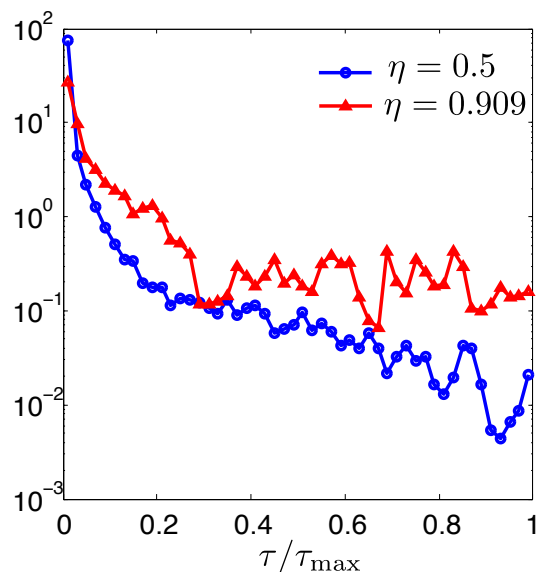| η	Q_1 (outward interactions)	Q_2 (ejections)	Q_3 (inward interactions)	Q_4 (sweeps)
0.5	23.9±1.2%	29.6±0.8%	22.8±0.9%	23.7±1.4%
0.909	17.2±0.9%	29.0±1.8%	21.8±%	32.0±1.5%

Figure 4. Normalised probability distribution function of the absolute value of the Reynolds stress (c.f. equation 1) in the 'Q' structures for $\eta = 0.5$ (circles) and $\eta = 0.909$ (triangles). For both cases $H = 1.75$; $\tau_{\max} = \max(\tau_i)$, where τ_i is the total Reynolds stress in an individual 'Q' structure

flow Lozano-Durán *et al.* [21] found that at least 60% of the total number of 'Q' structures were composed of Q_2 and Q_4's independent of the Reynolds number ($Re_\tau = 934, 2003$). In TC flow, Q_2 and Q_4's arise from the events leading to the formation of Taylor rolls i.e. the plume ejections from the inner cylinder which impact onto the outer cylinder and the plume ejections from the outer cylinder which are a result of the impact events. Both these events are strong markers of Q_2 and Q_4's respectively and from table 2 we find that when the curvature is low ($\eta = 0.909$) they account for almost 60% of the total 'Q's. In the case of a high curvature setup ($\eta = 0.5$) the percentage of Q_2's does not change significantly and the large scale structures observed in figure 3*b* belong to this quadrant. However, we find that the sweep events are drastically reduced. This is a consequence of less intense ejection events from the outer cylinder when $\eta = 0.5$ (c.f. figure 3*b*) which are crucial for the formation of Taylor rolls.

2.3. Reynolds stress distribution
In this subsection we look at how the tangential stresses are distributed among the 'Q' structures. We compute the total Reynolds stress in each 'Q' structure as the volume integral of the stress (c.f. equation 1) at each computational node enclosed in an individual structure. As seen
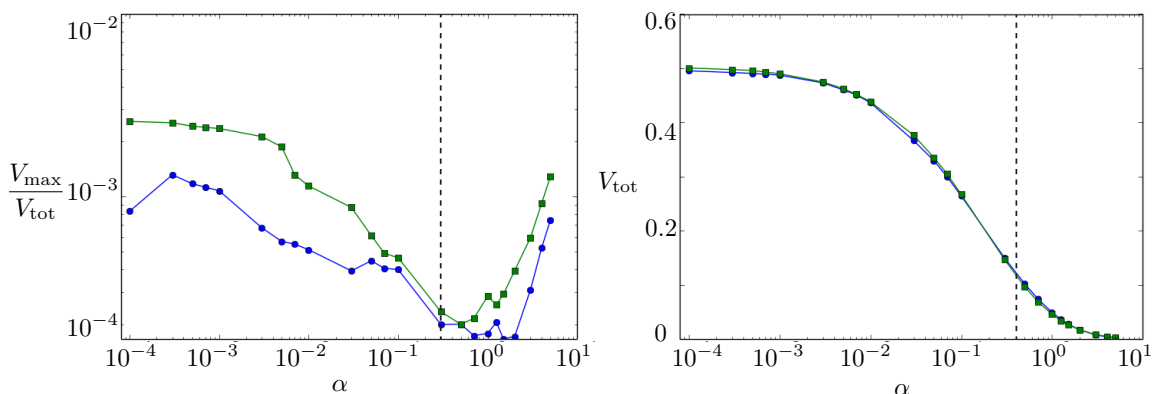
Figure 5. Left panel: Maximum volume of a vortex cluster normalised by the total volume of all the identified clusters in the domain. Right panel: Total volume of all the identified clusters in the domain. Square symbols refer to $\eta = 0.909$, while the circles refer to $\eta = 0.5$; dashed vertical line represents the chosen percolation parameter α

previously, structures in all four quadrants are present. Thus, structures which contain either positive or negative stresses are present, indicating the existence of both regions of ejecting herring-bone streaks, which detach from the boundary layer and form regions with on average, net positive transport, and impacting regions in the flow, where the structures originating from the other boundary layer impact the cylinder's boundary layer, and form regions of net negative transport. In figure 4 we plot histograms of the absolute value of normalised Reynolds stresses contained in the 'Q' structures for two different radius ratios to study the distribution of the Reynolds stress in the 'Q' structures. When the curvature is low ($\eta = 0.909$), we observe a uniform distribution of structures with high Reynolds stress ($0.6 < \tau/\tau_{\max} < 1$). These packets of large scale structures are responsible for majority of the angular velocity transport in a low-curvature setup. From the visualisation shown in figure 3 we observed that although small scale structures exist in both low and high curvature system, large scale rolls are more apparent when the curvature is low. On reducing H the large scale rolls merge forming large scale rolls which fill up the entire volume (c.f. figure 2). However when the curvature is high ($\eta = 0.5$), the probability to find structures with intense Reynolds stresses are much lower as compared to the case where $\eta = 0.909$.

3. Vortex clusters

3.1. Identification and percolation analysis

In this section we focus on the vortex clusters. A similar approach as in the previous section is adopted, where each vortex cluster is identified as a region satisfying the following criterion:

$$D(\mathbf{x}) > \alpha \overline{D'^2(r)}^{1/2}, \tag{2}$$

where $D(\mathbf{x})$ is the discriminant of the velocity gradient tensor at a single point, $\overline{D'^2}^{1/2}$ is the standard deviation of D over wall-normal planes while α is a thresholding parameter. Again, the thresholding parameter, in this case α has to be chosen carefully. A percolation analysis is done for vortex clusters as done for 'Q' structures in the previous sub-section, following the procedure by del Álamo *et al.* [20] for channel flows. Again, the connectivity of the vortex
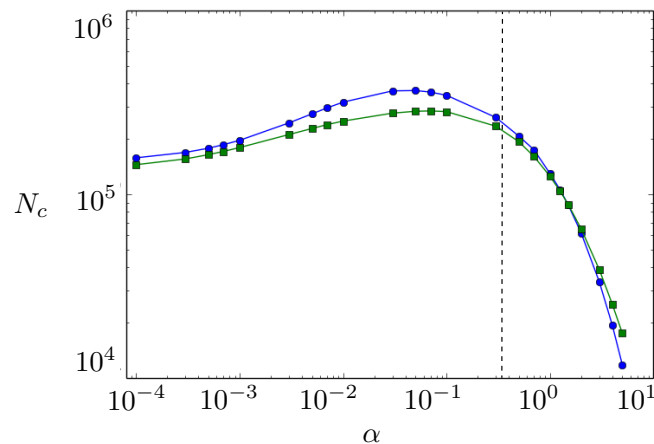
Figure 6. Total number of identified vortex clusters in the domain for two different radius ratios $\eta = 0.5$ (circles), $\eta = 0.909$ (squares); dashed vertical line represents the chosen percolation parameter α

clusters is defined in terms of its six neighbouring grid points and any object smaller than 30^3 wall units in volume is filtered out for the analysis.

In figure 5 we show the normalized maximum volume of a vortex cluster and the total volume of all the clusters for different values of α. The trend of $V_{\max}/V_{\text{tot}}$ for vortex clusters is similar to the one observed for 'Q' structures and a region of percolation crisis of the vortex clusters can also be identified around $\alpha_c \sim 0.08 - 0.1$. However, the maximum volume of any individual vortex cluster on reducing α does not go beyond 10^{-2} and the total volume occupied by these objects is roughly half of the total domain volume. This is an indication that the vortex clusters are much smaller objects as compared to the 'Q' structures. Following del Álamo *et al.* [20], we chose a percolation parameter of approximately $\alpha = 2.5\alpha_c$ i.e. $\alpha = 0.25$.

Figure 6 shows the total number of identified vortex clusters for different α. With increase in α, the total number of vortex clusters falls more steeply than the identified 'Q' structures with increase in H. An interesting observation is that the number of vortex clusters ($N_c \sim 10^5$) is much higher than that of 'Q' structures ($N_c \sim 10^3$; c.f. figure 1a) which shows that while the volume of individual vortex clusters is very small they are in much higher number as compared to the 'Q' structures.

3.2. Cluster geometries
As the volume of individual vortex cluster is extremely small compared to the total volume occupied by all the vortex clusters, it is challenging to analyze these clusters visually as done for the 'Q' structures. Instead, in this subsection we focus on the geometrical features of these vortex clusters. In the case of a turbulent channel flow, del Álamo *et al.* [20] found that the logarithmic region consists of small packs of clusters which are nearly homogenous and isotropic and another group of tall structures with their base in the near wall region ($y^+ \sim 20$). By circumscribing each vortex cluster with a parallelepipedal box, they found that the tall attached clusters are geometrically self-similar. We follow a similar approach and characterize the radial, axial and azimuthal lengths of each vortex cluster.

To characterize the geometry of the vortex clusters in the stream-wise ($\hat{\theta}$), wall-normal ($\hat{r}$) and span-wise ($\hat{z}$) directions, we compute the length of each cluster in three directions as
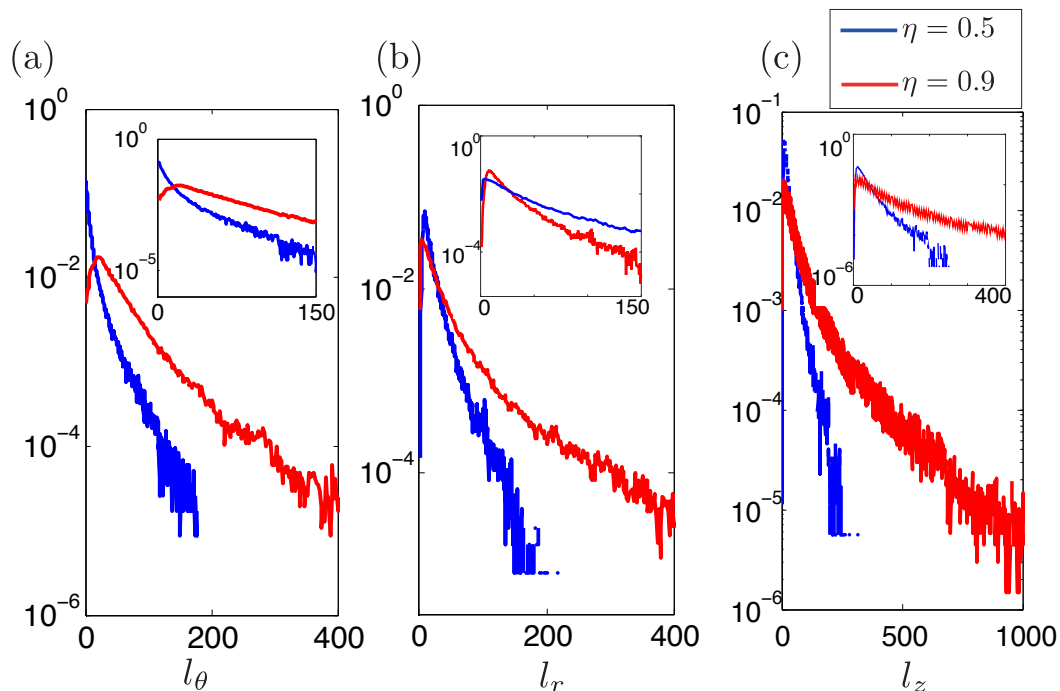
Figure 7. Probability distribution functions of the (a) stream-wise (l_θ) (b) wall-normal (l_r) and (c) span-wise (l_z) lengths of the vortex clusters. All lengths are computed in viscous wall units.

$l_i = \langle l_i \rangle_{\max} - \langle l_i \rangle_{\min}$. In figure 7, we plot the probability distribution functions of the lengths of these clusters for $\eta = 0.5$ and $\eta = 0.909$. Figure 7a shows that the stream-wise extent of the clusters is different for setups with different curvature. From the inset of figure 7a we find that it is more probable to find small scale stream-wise structures in a low-curvature setup ($\eta = 0.5$) as compared to a high curvature setup ($\eta = 0.909$). The radial and axial extents of the vortex clusters are much higher in a low-curvature setup as compared to a high-curvature setup. The stronger shear owing to the higher shear Reynolds number when $\eta = 0.909$ may be responsible for the vortex clusters to be larger as compared to when $\eta = 0.5$. We do not find any packets of self-similar clusters in the near wall region as observed by del Álamo *et al.* [20] in the case of a turbulent channel flow.

In order to study if these clusters have a preferential site of origin, we plot the joint probability distribution functions of the minimum and maximum radial and axial positions of the vortex clusters for both radius ratios in figure 8. While del Álamo *et al.* [20] found groups of tall structures originating from the near wall region in case of TC flow we find that the clusters are of uniform wall-normal lengths throughout the domain in case of both $\eta = 0.5$ and $\eta = 0.909$. The origin of this effect is unclear and further analysis is required in understanding the formation of the vortex clusters in TC flow. Additionally, the clusters in $\eta = 0.909$ case are at least twice the length of the clusters when $\eta = 0.5$.

3.3. Dissipation in vortex clusters

Similar to the analysis done in section 2.3, here we compute the total dissipation in each vortex cluster as a volume integral of the net dissipation at every computational grid node enclosed in each vortex cluster i.e $\epsilon = \frac{\int \epsilon_i dV}{\int dV}$, where ϵ_i is the dissipation computed in a computational box
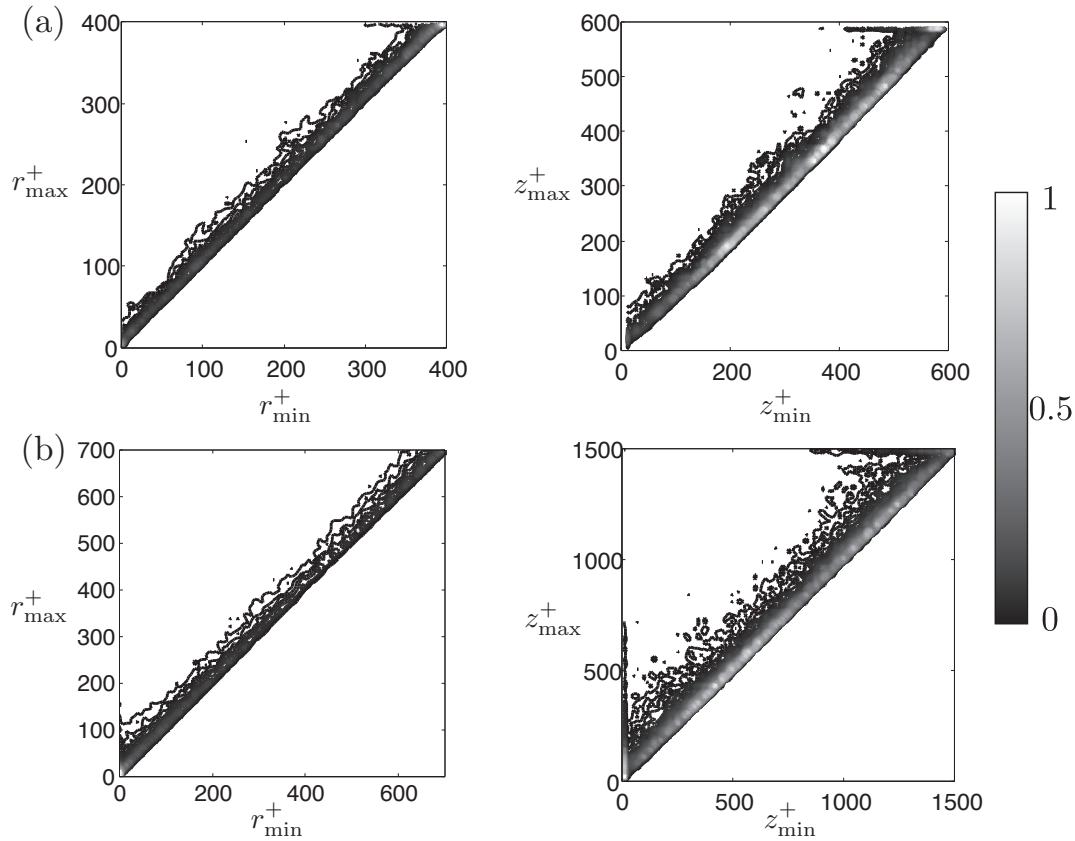
Figure 8. Joint probability distribution functions to describe the geometry of the vortex clusters (a) $\eta = 0.5$ (b) $\eta = 0.909$. The plot is in greyscale and the color scale varies from 0 to 1 in each plot; dark colour indicates lower probability while a lighter colour refers to high probability.

of volume dV. The result is shown in figure 9. Contrary to figure 4, in the case of vortex clusters we observe almost no differences in the net dissipation contained in each vortex cluster between both cases. Although the low curvature setups have taller/longer vortex cluster extending in the wall-normal direction, as observed from figure 8, the distribution of the dissipation in these clusters is almost homogenous, and very few clusters have extreme dissipation. Additionally the difference in the p.d.f of the dissipation in the vortex clusters for three different snapshots of the flow is less than 5 %.

4. Summary and outlook

The study of formation, evolution and decay of coherent structures in wall bounded turbulent flows is crucial for our understanding of the complex multi-scale process of turbulence. While many previous studies have focussed on gaining insight on the role of these coherent structures in canonical flow setups such as pipe flow or channel flows, other flows where the curvature of the wall is along the direction of the streamlines have been hardly investigated. In this work we consider such a system, i.e. Taylor-Couette (TC) flow, where the flow is driven between two independently rotating co-axial cylinders. By following the approach of Lozano-Durán *et al.* [21] and del Álamo *et al.* [20] we have developed suitable criteria and identified Reynolds stress structures ('Q's') and vortex clusters in a turbulent Taylor-Couette flow.

    Through the analysis of single flow-field snapshots of two different radius ratios ($\eta = 0.5$, and
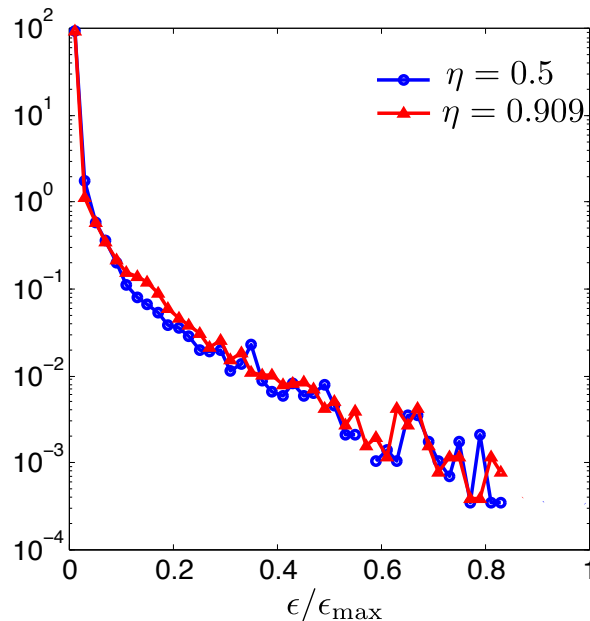
Figure 9. Normalised probability distribution function of the total dissipation in the vortex structures for $\eta = 0.5$ (circles) and $\eta = 0.909$ (triangles).

$\eta = 0.909$) we find, consistent with previous analysis, that low-curvature TC systems have wall-attached, large-scale Taylor rolls which fill up the entire volume, and transport the majority of Reynolds stresses. This is a further way of quantifying the existence of these structures, which have also been observed in the time averaged contours, axial autocorrelations and velocity spectra. Unlike the case of channels, where different results were found for the transport of the large-scales when applying the 'Q 'analysis [21], here, the results obtained are consistent with previous results from co-spectra [13].

When the curvature is high, the large-scale rolls break up into smaller structures, herringbone-like streaks and the flow structure is more similar to what is seen in other wall-bounded turbulent flows. Contrary to the 'Q's, we find that vortex clusters are much higher in number. While the 'Q's fill up the entire volume of the domain, the vortex clusters occupy a much smaller volume, and, in general are smaller and thus come in higher numbers. The distribution of the sizes of the vortex clusters is mostly homogenous and no groups of wall-attached and wall-detached clusters are found in TC flow for both the low-curvature and high-curvature systems. The clusters are found to be larger for the $\eta = 0.909$ case, however, dissipation statistics did not change between both cases.

During the Multiflow Summer workshop, due to time constraints and due to limited computational resources this analysis was applied to relatively small boxes of $(6.2 \times 2 \times 4.2)d/2$ at moderate frictional Reynolds numbers $Re_\tau \approx 400$. We plan on extending this analysis to small boxes at frictional Reynolds numbers up to $Re_\tau \approx 3000$, and also to large computational boxes of up to $(24 \times 2 \times 16)d/2$, and to a larger number of flowfield napshots to reduce the statistical errors, and to be able to separate the Qs into their quadrants while obtaining useful information about their physics. Further analysis at other radius ratio or for counter-rotating cylinders will be useful to determine the validity of the obtained insights.

Acknowledgments

References

[1] Pope S B 2000 *Turbulent Flow* (Cambridge U. Press)
[2] Smits A J, McKeon B J and Marusic I 2011 *Annu. Rev. Fluid Mech.* **43** 353–375
[3] Townsend A E 1980 *The structure of turbulent shear flow* (Cambridge U. Press)
[4] Perry A E and Chong M S 1982 *J. Fluid Mech.* **119** 173–217
[5] Perry A E, Henbest S M and Chong M S 1986 *J. Fluid Mech.* **165** 163–199
[6] Jiménez J 2011 *Annu. Rev. Fluid Mech.* **44** 27
[7] Grossmann S, Lohse D and Sun C 2016 *Annu. Rev. Fluid Mech.* **48**
[8] Avsarkisov V, Hoyas S, Oberlack M and García-Galache J P 2014 *J. Fluid Mech.* **751** R1–8
[9] Bradshaw P 1973 Effects of streamline curvature on turbulent flow. *Agardograph* AG-169 (AGARD)
[10] Hunt I A and Joubert P N 1979 *J. Fluid Mech.* **91** 633–659
[11] Hoffmann P H, Muck K C and Bradshaw P 1985 *J. Fluid Mech.* **161** 371–403
[12] Huisman S G, van der Veen R C, Sun C and Lohse D 2014 *Nature Communications* **5** 3820
[13] Ostilla-Mónico R, Verzicco R, Grossmann S and Lohse D 2015 *J. Fluid Mech.* **788** 95–117
[14] Ostilla-Mónico R, van der Poel E, Verzicco R, Grossmann S and Lohse D 2014 *J. Fluid Mech.* **761** 1–26
[15] van der Veen R, Huisman S, Merbold S, Harlander U, Egbers C, Lohse D and Sun C 2015 *arXiv:1508.05802*
[16] Wallace J M, Eckelmann H and Brodkey R S 1972 *J. Fluid Mech.* **54** 39–48
[17] Lu S S and Willmarth W W 1973 *J. Fluid Mech.* **60** 481–511
[18] Willmarth W W and Lu S S 1972 *J. Fluid Mech.* **55** 65–92
[19] Chong M S, Perry A E and Cantwell B J 1990 *Phys. Fluids* **2** 765–777
[20] del Álamo J, Jiménez J, Zandonade P and Moser R D 2006 *J. Fluid Mech.* **561** 329–358
[21] Lozano-Durán A, Flores O and Jiménez J 2012 *J. Fluid Mech.* **694** 100–130
[22] Verzicco R and Orlandi P 1996 *J. Comput. Phys.* **123** 402–414
[23] van der Poel E P, Ostilla–Mónico R, Donners J and Verzicco R 2015 *Comput. Fluids* **116** 10–16
[24] Ostilla–Mónico R, Stevens R, Grossmann S, Verzicco R and Lohse D 2013 *J. Fluid Mech.* **719** 14–46
[25] Ostilla–Mónico R, Huisman S G, Jannink T, Van Gils D, Verzicco R, Grossmann S, Sun C and Lohse D 2014 *J. Fluid Mech.* **747** 1–29
[26] Ostilla–Mónico R, van der Poel E, Verzicco R, Grossmann S and Lohse D 2014 *Phys. Fluids* **26** 015114
[27] Eckhardt B, Grossmann S and Lohse D 2007 *J. Fluid Mech.* **581** 221–250